Modeling Wideband Radiated Emissions From PCBs in Shielding Enclosures Based on Single-Plane Phaseless Near-Field Scanning

Zhifei Xiao[®], Zi An Wang[®], *Graduate Student Member, IEEE*, Li Jun Jiang[®], *Fellow, IEEE*, and Ping Li[®], *Senior Member, IEEE*

Abstract—This article presents a wideband phaseless source reconstruction method (SRM) for the evaluation of the radiated emissions from printed circuit boards (PCBs) in shielding enclosures. The PCBs are modeled with equivalent dipoles, and the numerical Green's function (NGF) is deployed to establish the relationship between the equivalent source and the input near-field (NF) data, thus the electromagnetic influences of the surrounding environments comprehensively accounted. This method only requires magnitude-only NF scanning over a single plane, thus significantly decreasing the NF measurement difficulty. To remedy the lack of phase information of the NF data, the input NF data are equally divided into two groups with a uniform distribution strategy, and then the phase of NF data can be retrieved via an iterative approach. Moreover, with the objective of improving the convergence of the iterative SRM procedure, the initial phase of the NF data is set as the same as the NGF. In addition, a cubic-splinealgorithm-enhanced adaptive frequency sampling strategy is applied for source reconstruction in a wide frequency band, which avoids repetitively implementing the SRM at every frequency, thus saving a large amount of CPU time. To validate the effectiveness of the proposed wideband phaseless SRM, several representative numerical examples are investigated, in which both the NF and the far-field radiated emission are evaluated.

Index Terms—Adaptive frequency sampling (AFS), numerical Green's function (NGF), phase retrieval, printed circuit boards (PCBs) in shielding enclosure, single-plane phaseless near-field (NF) scanning, Tikhonov regularization, wideband phaseless source reconstruction.

I. INTRODUCTION

HE increase of integration level and complexity of modern electronic systems has brought about more challenges to electromagnetic compatibility (EMC) and electromagnetic interference (EMI) design. Radiated emission tests are necessary for the analysis of EMI problems. However, standard far-field (FF) tests performed in the open-area test site or semi-anechoic

Manuscript received 12 October 2023; revised 7 January 2024; accepted 3 February 2024. Date of publication 19 February 2024; date of current version 13 June 2024. This work was supported by NSFC under Grant 62071290. (Corresponding author: Ping Li.)

Zhifei Xiao, Zi An Wang, and Ping Li are with the State Key Laboratory of Radio Frequency Heterogeneous Integration, Shanghai Jiao Tong University, Shanghai 200240, China (e-mail: ping.li@sjtu.edu.cn).

Li Jun Jiang is with the Department of Electrical Engineering, Missouri University of Science and Technology, Rolla, MO 65409 USA.

Color versions of one or more figures in this article are available at https://doi.org/10.1109/TEMC.2024.3362960.

Digital Object Identifier 10.1109/TEMC.2024.3362960

chambers require a high cost of time and money [1]. As a result, near-field (NF) to FF transformation algorithms based on convenient NF measurements have been developed to solve the problem [2].

Source reconstruction method (SRM) is a popular technique widely applied to NF–FF transformations [3], [4], [5]. The radiated field at any point in free space can be calculated by reconstructing the equivalent source over the surface of a device under test (DUT) from NF data [6]. With the assistance of SRM, the original circuit structure can be replaced by equivalent currents or dipoles while generating the same electromagnetic radiation [7]. Compared to continuous equivalent currents, discrete equivalent dipoles are generally more often used in practical EMC problems for less computational cost. In addition, the equivalent dipole model can be easily imported into full-wave simulation software for further analysis [8].

Shielding enclosures are widely used to suppress EMI in practical engineering scenarios. Modeling radiated emissions from printed circuit boards (PCBs) inside the enclosure is a challenging problem. A dipole-dielectric-conducting equivalent source model is proposed in [9], which is reconstructed in free space, and then, placed in the shielding enclosure for radiated emission estimation. However, the effects of the shielding enclosure are not considered in the source reconstruction process, which degrades the reconstruction accuracy. The SRM in [10] uses equivalent electric and magnetic currents expanded by the Rao-Wilton-Glisson (RWG) basis function to model the radiated emissions, while it has the same limitation. In [11], a novel NGF-based SRM is proposed to accurately characterize the emissions of electronic circuits within shielding enclosures. The NGF is used in this method to establish the relationship between equivalent dipole moments and input NF data. This model takes the coupling between the board and the shielding enclosure into consideration, which addresses limitation of previous models. This method can not only accurately calculate the radiation FF outside the shielding enclosure but also effectively predict the NF inside the cavity. However, it should be noted that this method is applicable only for the NF data that includes both amplitude and phase information.

The aforementioned SRMs require both magnitude and phase information to build up a linear relationship between the input NF data and equivalent source. However, the acquisition of phase information requires more complicated measurement and

 $0018-9375 © 2024 \ IEEE. \ Personal \ use is permitted, but republication/redistribution \ requires \ IEEE \ permission.$ See https://www.ieee.org/publications/rights/index.html for more information.

calibration process compared with direct magnitude measurements [12]. Accurate phase measurements are difficult to realize at high frequencies. As a result, SRM based on magnitude-only NF data has gradually become a research focus. The lack of phase information results in a set of nonlinear equations in the source reconstruction process, which brings about great challenges to obtaining accurate solutions. A common approach to solving nonlinear problems is using global optimization algorithms, such as genetic algorithms [13], differential evolution algorithms [14], and particle swarm optimization algorithms [15]. However, the computational cost of these global optimization algorithms increases dramatically with the increase of unknowns, i.e., the number of equivalent sources. For complex electronic circuits requiring a large number of equivalent dipoles, the global optimization algorithms are not applicable. Another effective method to solve this problem is phase retrieval. In [16] and [17], the missed phase information is retrieved in an iterative fashion using the NF data sampled from two parallel planes. In this way, the number of equivalent dipoles is unlimited. However, it is time consuming to perform NF scanning over two planes. Neural networks have been employed in phaseless SRMs due to their powerful capability of handling nonlinear problems [18], [19], while they also require two-plane NF scanning for the effective training. An improved SRM based on single-plane NF scanning is proposed in [20]. By interpolating the sampled NF, two groups of NF data are obtained, i.e., the sampling group and interpolation group. The parameters of equivalent dipoles are determined through an iteration process between the two groups, where the singular value decomposition algorithm is used to solve the inverse problem. The SRM proposed in [21] offers a convenient approach as it also only necessitates phaseless NF data acquired from a single plane in order to solve equivalent sources. This method constructs a nonlinear cost function based on integral equations, and utilizes the Born iteration algorithm and regularization techniques to minimize the cost function and obtain a solution for the ill-posed nonlinear system. With the assistance of this method, there is no need for iterative calculations between two sets of NF data to solve the equivalent source. These methods only require NF scanning over a single plane, thus shortening the scanning time to half of conventional methods. However, no such methods have been developed for phaseless SRM in shielding environments.

In practical application, it is necessary to evaluate radiated emissions in a wide band. However, the direct implementation of SRM at multiple frequency points result in repetitive computations and prohibitive computational cost. The wideband SRM proposed in [22] uses the Stoer–Bulirsch algorithm with adaptive frequency sampling (AFS) to interpolate the reconstructed equivalent sources at some preset frequency points and obtains the equivalent source model in a whole frequency band. A wideband phaseless SRM is proposed in [23], where the parameters of equivalent dipoles are determined using the differential evolution algorithm. The phaseless NF scanning is performed at three preset frequency points. The equivalent source at any frequency point in a wide band is solved by interpolating the equivalent source at the aforementioned predetermined frequency points. However, the effectiveness of the algorithm in reconstructing the radiated field of electronic circuits inside a shielding enclosure

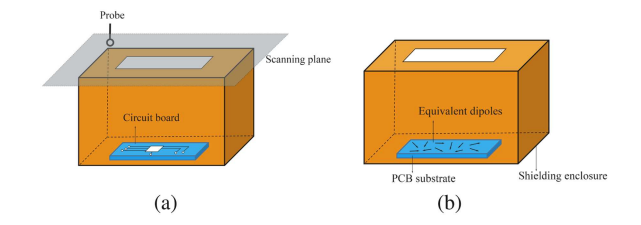


Fig. 1. Geometry of the proposed equivalent source model of the PCB in the shielding enclosure. (a) Geometry of the original circuit model in the shielding enclosure. (b) Geometry of the proposed equivalent dipole model.

In this article, a wideband SRM merely relying on singleplane phaseless NF scanning is proposed to characterize radiated emissions from PCBs in shielding enclosures. In the proposed phaseless SRM, only the magnitude of the NF data over a single plane is required, thereby dramatically alleviating the NF sampling difficulty and simultaneously reducing the NF sampling time. To imitate the realistic electromagnetic (EM) environments, the NGF [24] taking into account the electromagnetic effects of the shielding enclosure is deployed to build up the relationship between the sampled NF data and the reconstructed equivalent source located in the shielding enclosure. In order to treat the lack of phase information, the sampled NF data are equally divided into two groups, then the phase information can be retrieved using an iteration method. Besides, with the aim to speed up the convergence of the iterative SRM, the initial phase of the NF data is set as same as the NGF. In addition, for wideband radiators, an effective wideband equivalent source model is achieved through the use of cubic spline interpolation algorithm together with adaptive frequency sampling (AFS). The proposed SRM enables effective estimation of the wideband radiated emissions from PCBs in shielding enclosures via single-plane NF scanning.

The rest of this article is organized as follows. Section II elaborates on the methodology. Section III presents three numerical examples to validate the proposed method for both NF and FF reconstruction. Finally, Section IV concludes this article.

II. METHODOLOGY

The proposed wideband phaseless SRM consists of two steps. In the first step, an iterative strategy is applied to recover the phase information of the magnitude-only near-field scanning data. In the second step, an AFS-assisted interpolation method is employed to obtain a wideband equivalent source model, thus enabling the estimation of radiated emissions in a wide frequency band. In this section, the two steps are described in detail.

A. Iteration Method for Phase Retrieval

As illustrated in Fig. 1(a), the circuit board is placed within a shielding enclosure in the original scenario. The NF data are measured over a plane above the shielding enclosure by a magnetic loop probe. As shown in Fig. 1(b), an array of oriented equivalent magnetic dipoles with arbitrary polarization direction serving as the equivalent source is directly placed over the substrate surface of the PCB located inside a shielding enclosure.

the substrate, and the shielding enclosure are fully considered. To simplify the computation, each equivalent magnetic dipole is decomposed into two components: x-component \mathbf{M}^x and y-component \mathbf{M}^y . Then, the radiated magnetic field generated by a magnetic dipole can be expressed as follows [25]:

$$\mathbf{H}(\mathbf{r}) = \overline{\overline{\mathbf{G}}}(\mathbf{r}, \mathbf{r}') \cdot \mathbf{M} \tag{1}$$

where $\overline{\overline{G}}(\mathbf{r},\mathbf{r}')$ is a Dyadic Green's function (DGF), and \mathbf{r} and \mathbf{r}' are positions of measurement point and source point, respectively. Due to unavailability of analytical form of the DGF in complex EM environment, a numerical Green's function (NGF) is deployed. In this work, the DGF is calculated by the method of moments (MoM) algorithm [26]. According to (1), the relationship between equivalent dipoles and input NF data can be established by point matching as follows:

$$GM = H (2)$$

where **G** is the matrix of NGF for equivalent dipole components, **M** is moments of equivalent dipoles, and **H** denotes the sampled magnetic NF data obtained from single-plane NF scanning. To ensure accuracy of solution of (2), the number of measurement points is usually set as larger than the number of equivalent dipoles. As a result, the solution of (2) is overdetermined. Thus, the least-square method (LSM) is applied to solve this overdetermined equation as follows:

$$\hat{\mathbf{M}} = \underset{\mathbf{M}}{\operatorname{arg\,min}} \|\mathbf{G}\mathbf{M} - \mathbf{H}\|^2 \tag{3}$$

where $\| \bullet \|$ is the Euclidean norm. Due to the ill-posed property of the inverse problem, the solution of (2) is sensitive to variation of the coefficients in the equation [27]. To overcome this problem, the Tikhonov regularization technique is applied by adding a quadratic penalty term based on (3) as follows [28]:

$$\hat{\mathbf{M}} = \underset{\mathbf{M}}{\operatorname{arg\,min}} \|\mathbf{G}\mathbf{M} - \mathbf{H}\|^2 + \mu \|\mathbf{L}\mathbf{M}\|^2$$
 (4)

where L is Tikhonov matrix, which is nonnegative and semidefinite, and μ represents the regulation parameter that controls the relative weight of the penalty term with a positive value. If the null spaces of G and L intersect trivially, then the closed form of M in (3) can be expressed as follows [29]:

$$\hat{\mathbf{M}} = \left(\mathbf{G}^{\dagger}\mathbf{G} + \mu\mathbf{L}\right)^{-1}\mathbf{G}^{\dagger}\mathbf{H} \tag{5}$$

where the superscript † indicates complex conjugate transpose. When the value of $\mu = 0$, the form of (5) simplifies to the standard form of solution obtained through the traditional LSM, which is shown in (3).

In this article, the standard form of Tikhonov regularization is utilized to effectively solve the ill-posed inverse problem, where ${\bf L}$ is set as the identity matrix. The Tikhonov regularization technique is highly effective in mitigating the impact of noise and measurement errors in source reconstruction problems. Generalized cross validation (GCV) is applied to seek the optimal choice of regularization parameter μ in (5) as follows [29]:

$$\mu_{GCV} = \arg\min \mathbf{G}(\mu) \tag{6}$$

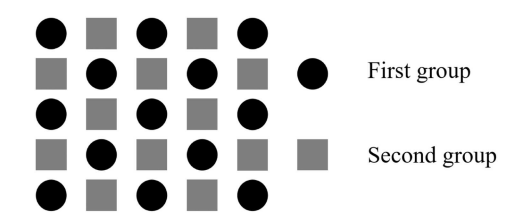


Fig. 2. Illustration of the partition of sampled NF data for the following iterative phase retrieval.

while

$$\mathbf{G}(\mu) = \frac{\|(\mathbf{I} - \mathbf{A}(\mu))\mathbf{H}\|^2}{\{tr(\mathbf{I} - \mathbf{A}(\mu))\}^2}$$
(7)

and

$$\mathbf{A}(\mu) = \mathbf{G} \left(\mathbf{G}^{\dagger} \mathbf{G} + \mu \mathbf{L} \right)^{-1} \mathbf{G}^{\dagger} \tag{8}$$

where **I** is identity matrix. Since the closed form of μ cannot be expressed directly, an approximate value of μ is found from a set of likely values by evaluating $\mathbf{G}(\mu)$. In the proposed method, the golden section search technique [30] is utilized to effectively search for the optimal value of μ .

In the proposed model, the sampled NF data contains only magnitude information. As a result, (2) becomes nonlinear. To address this issue, a novel iteration method is developed to retrieve phase information from magnitude-only NF data. As shown in Fig. 2, the NF data obtained from the scanning plane are evenly divided into two groups in terms of the spatial position of the sampling points, where the NF data in two groups appears alternatively and both are distributed in the whole NF sampling region, which ensure every group data possess a global property. In the first step of iteration method, an assumed initial phase is added to the first group of NF data. It is important to note that the accuracy of the assumed initial phase plays a crucial role in ensuring the convergence of the proposed iteration method [31]. In many previous works, the initial phase is commonly set as zero [16], [20]. However, in this work, the initial phase of NF data is set as the same as NGF, which strikingly improves the convergence performance of the phaseless source reconstruction process. The effectiveness of this phase initialization strategy is presented in Section III.

After making the initial phase assumption, (2) can be solved directly using the aforementioned Tikhonov regularization technique combined with GCV based on NF data of the first group. However, at the early stage of the iteration process, the solution of the equivalent source may be inaccurate due to the lack of phase information of sampled NF data. To evaluate the accuracy of reconstructed NF data, an error function is defined as follows:

$$\sigma = \frac{\||\mathbf{H}^{\text{new}}| - |\mathbf{H}^{\text{meas}}|\|}{\||\mathbf{H}^{\text{meas}}|\|}$$
(9)

where \mathbf{H}^{meas} represents the NF data obtained from NF scanning, \mathbf{H}^{new} represents the NF data calculated by the equivalent source obtained from the proposed iteration method, and $|\bullet|$ denotes magnitude of field data. If the value of the error function σ described previously satisfies a predefined stop criterion σ_t or the predefined iteration number is achieved, the iteration process will be terminated. Otherwise, the magnitude of the calculated

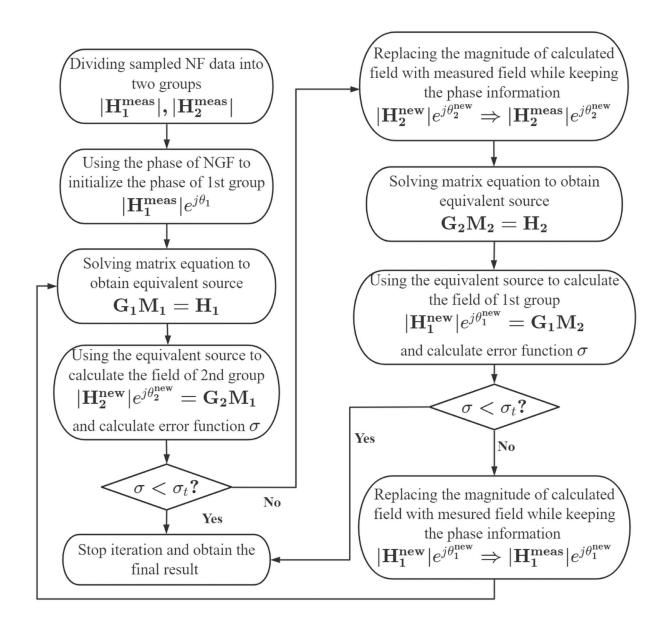


Fig. 3. Flowchart of the proposed iteration method to retrieve phase information from magnitude-only NF data.

NF data will be replaced by the measured field, while the phase information will be retained after completing one iteration step, i.e., $|\mathbf{H}^{\text{new}}|e^{j\phi^{\text{new}}} \Rightarrow |\mathbf{H}^{\text{meas}}|e^{j\phi^{\text{new}}}$. The detailed process of the proposed iteration method is shown in Fig. 3. The equivalent source at any single frequency point within the entire working band can be obtained by following the iteration steps mentioned previously.

B. Interpolation Algorithm for the Wideband SRM

The equivalent dipole sources acquired in Section II-A allow for the estimation of radiated emissions at the investigated frequency point. Nevertheless, the electronic devices typically operate over a wide frequency range. To achieve the wideband radiated emission modeling, the cubic spline interpolation algorithm is employed in this work [30]. This algorithm is a powerful numerical method used to approximate smooth curves based on a given set of data points. Its effectiveness is particularly notable in solving wideband source reconstruction problems.

In the proposed method, the cubic spline interpolation algorithm is directly applied to the acquired equivalent sources at a predetermined set of supporting frequency points, denoted as f_1, f_2, \dots, f_n . The equivalent dipole moments at the corresponding frequency points are defined as $M_1, M_2, ..., M_n$, respectively. Then, the equivalent dipole moments can be decomposed to real part and imaginary part as $\mathbf{M}_i = \mathbf{m}_i^r + j\mathbf{m}_i^i$ (i = 1, 2, ..., n), where \mathbf{m}_i^r is the real part of \mathbf{M}_i and \mathbf{m}_i^i is the imaginary part of M_i . Then, the interpolation function for real part $S_r(f)$ and imaginary part $S_i(f)$ is constructed, respectively. Finally, the equivalent dipole moment can be obtained by $S(f) = S_r(f) + jS_i(f)$. Here, $S_r(f)$ is taken as an example to demonstrate the solution of the interpolation function. The function $S_r(f)$ can be expressed as a piecewise function consisting of cubic polynomials that ensure consecutive first and second derivatives. We can define the function as follows

$$\begin{split} &(i=1,2,\ldots,n-1);\\ &\mathbf{S}_r^i(f)=a_i(f-f_i)^3+b_i(f-f_i)^2+c_i(f-f_i)+d_i \quad (10)\\ &\text{where } \mathbf{S}_r^i(f)\text{ satisfies following condition:}\\ &\mathbf{S}_r^i(f_i)=\mathbf{m}_i^r \quad (i=1,2,\ldots,n-1)\\ &\mathbf{S}_r^i(f_{i+1})=\mathbf{m}_{i+1}^r \quad (i=1,2,\ldots,n-1)\\ &\mathbf{S}_r^{i'}(f_{i+1})=\mathbf{S}_r^{i+1'}(f_{i+1}) \quad (i=1,2,\ldots,n-2) \end{split}$$

Then, the global interpolation function can be written as $\mathbf{S}_r(f) = \mathbf{S}_r^i(f)$ $(i=1,2,\ldots,n-1)$ for $f_i \leq f \leq f_{i+1}$. Similarly, $\mathbf{S}_i(f)$ can also be determined using the same interpolation method. Therefore, it is possible to construct a smooth curve that passes through all the supporting frequency points. As a result, the cubic spline interpolation algorithm provides a smooth and continuous approximation to the equivalent dipole moments in a wide band.

 $S_r^{i''}(f_{i+1}) = S_r^{i+1''}(f_{i+1}) \quad (i = 1, 2, ..., n-2).$

To enhance the efficiency of the interpolation algorithm, an AFS strategy [22] is employed in this work. The AFS is a bisection process until a termination criterion is achieved, which helps optimize the interpolation process and minimize the number of frequency points required in the interpolation algorithm. First, a coarse initial frequency step Δf is set to generate frequency points that are uniformly distributed throughout the entire working band. The solutions of (2) at these frequency points are kept as the initial data of the cubic spline algorithm. Then, the new frequency points f_{new} are generated by $f_{\text{new}} = \frac{f_i + f_{i+1}}{2}$ at every subinterval (f_i, f_{i+1}) , i = 1, 2, ..., n-1. After generating the new frequency points f_{new} , the equivalent dipole moments obtained by solving (2) at f_{new} are denoted as \mathbf{M}_{new} and the solutions obtained from the cubic spline interpolation algorithm at corresponding frequency points are denoted as M_c . To determine whether the bisection process can be terminated, an error function is defined as follows:

$$\sigma = \frac{\|\mathbf{M}_{\text{new}} - \mathbf{M}_c\|}{\|\mathbf{M}_{\text{new}}\|}.$$
 (11)

When the error function σ becomes smaller than the predefined threshold ε , the bisection process is terminated in the current subinterval, and then, moves to next subinterval. After the convergence criterion is achieved in every subinterval, all generated frequency points are kept as supporting points for the cubic spline interpolation algorithm. Finally, the equivalent source at any frequency point in the working band can be obtained by applying cubic spline interpolation algorithm with the aforementioned supporting frequency points determined by the AFS strategy.

The entire procedure of the proposed wideband SRM based on magnitude-only NF data can be summarized as follows:

- 1) Setting an initial sampling interval Δf to generate uniformly distributed frequency points and obtaining magnitude-only NF data from one sampled plane at aforementioned frequency points.
- 2) Dividing the sampling NF data into two groups according to the method shown in Fig. 2. Performing iteration steps

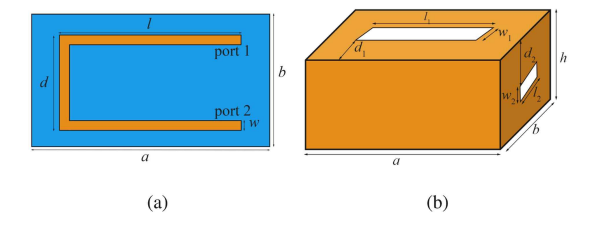


Fig. 4. (a) Geometry of the PCB in the first numerical example $(a=10~{\rm cm},b=5~{\rm cm},l=8~{\rm cm},d=4~{\rm cm},$ and $w=3.58~{\rm mm})$. (b) Structure of the shielding enclosure with two slots $(a=15~{\rm cm},b=10~{\rm cm},h=5~{\rm cm},l_1=6~{\rm cm},d_1=3.5~{\rm cm},w_1=3~{\rm cm},l_2=3~{\rm cm},d_2=1.75~{\rm cm},$ and $w_2=1.5~{\rm cm})$.

proposed in Section II-A based on the aforementioned two groups of NF data. Finally, solving for the equivalent source at every sampling frequency point obtained from step 1.

- 3) Using interpolation algorithm integrated with the AFS technique proposed in Section II-B to effectively determine the set of supporting frequency points.
- 4) Using the cubic spline interpolation algorithm based on supporting frequency points obtained from step 3 to calculate moments of equivalent dipoles at arbitrary frequency point in the working band. Then, the radiated NF and FF of electronic circuits placed in shielding enclosure can be reconstructed with the proposed method. Then, the radiated field generated by the original circuit structure including NF and FF can be obtained by full-wave simulations or calculated according to the relationship in (2).

III. NUMERICAL RESULTS

In this section, three numerical examples are shown to validate the proposed SRM in near- and far-field reconstruction. The working frequency is set as from 1 to 4 GHz and the initial sampling interval Δf is set as 500 MHz. The equivalent dipoles are equally placed over the substrate of the PCB with the number equal to 25. The x-component and y-component of the magnetic NF data are sampled as the inputs of the proposed SRM. The input NF data are set with sufficient sampling number to ensure the accuracy of the algorithm while considering sampling cost at the same time. The size of the sampling plane is set as $1.5\sim2$ times larger than the size of substrate to collect sufficient electromagnetic information [10]. Due to the lack of NF measurement equipment, the sampled NF data in this work are obtained via full-wave simulation by a commercial software FEKO. The effectiveness of the proposed phase initialization method is also investigated.

A. PCB With a C-Shaped Transmission Line in a Shielding Enclosure With Two Slots

In this example, a PCB with a C-shaped line is shown in Fig. 4(a). A 1-V voltage source is placed at port 1, while a 50- Ω resistor is terminated at port 2, which is the same as the source resistance. The thickness of the substrate is 2 mm. The material of the substrate is FR4 with the ε_r of 4.35. The transmission lines on the PCB are assumed to have zero thickness and infinity conductivity. As shown in Fig 4(b), the PCB is positioned centrally

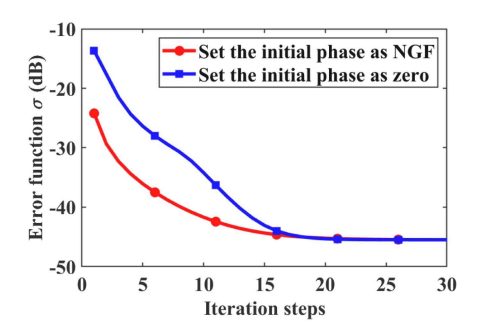


Fig. 5. Reconstructed error (in decibel) of two different phase initialization methods in the first numerical example.

TABLE I
INTERPOLATION ERROR OF THE PROPOSED SRM AT CENTRAL FREQUENCY
POINTS OF EVERY SUBINTERVAL IN THE FIRST NUMERICAL EXAMPLE

f (GHz)	1.0625	1.1875	1.3125	1.4375	1.5625	1.6875
$\sigma(\%)$	1.96	5.42	4.24	4.75	5.3	0.85
f (GHz)	1.875	2.125	2.3125	2.40625	2.46875	2.53125
$\sigma(\%)$	5.02	1.35	5.67	1.46	5.12	4.47
f (GHz)	2.59375	2.6875	2.8125	2.90625	2.96875	3.0625
$\sigma(\%)$	1.01	3.15	5.31	4.67	4.92	2.55
f (GHz)	3.15625	3.21875	3.3125	3.40625	3.46875	3.53125
$\sigma(\%)$	4.89	5.61	5.23	1.92	0.77	3.42
f (GHz)	3.59375	3.6875	3.8125	3.9375		
$\sigma(\%)$	2.66	5.34	5.47	4.76		

above the inner bottom of a shielding enclosure with two slots at top surface and right surface, respectively. The thickness of the shielding enclosure is set as 2 mm. The input NF data are sampled from a plane 6 cm with the size of $20 \text{ cm} \times 15 \text{ cm}$ above the ground plane. The number of sampling NF points is 1 271 with the resolution of 5 mm.

The comparison of the aforementioned two phase initialization methods is shown in Fig. 5. It is evident that our proposed phase initialization method leads to a faster convergence rate compared to simply setting the initial phase as zero.

In this example, the supporting frequency points are $f_s = \{1, 1.125, 1.25, 1.375, 1.5, 1.625, 2, 2.25, 2.375, 2.4375, 2.5, 2.5625, 2.625, 2.75, 2.875, 2.9375, 3, 3.125, 3.1875, 3.25, 3.375, 3.4375, 3.5, 3.5625, 3.625, 3.75, 3.875, 4} GHz. The error functions defined in (11) at the midpoint of every subinterval generated by the above supporting frequency points are shown in Table I. The average value of the error function <math>\sigma_{\text{mean}}$ is 3.83%.

To have a quantitative understanding of the accuracy of the reconstructed field calculated by the equivalent source, a mean-squared-error (mse) function is defined as follows:

$$\sigma_{\text{mse}} = 20 \log \frac{\||\mathbf{H}_{\text{cal}}(\mathbf{r})| - |\mathbf{H}_{\text{ref}}(\mathbf{r})|\|}{\||\mathbf{H}_{\text{ref}}(\mathbf{r})|\|}$$
(12)

where \mathbf{H}_{cal} and \mathbf{H}_{ref} are magnetic field data calculated by the proposed SRM and FEKO simulation, respectively. The reconstructed equivalent source at the frequency 1.6875 GHz is taken as an example to demonstrate the accuracy of the proposed SRM. To validate the proposed SRM in NF reconstruction, the magnetic NF data are sampled from another plane 7 cm above the ground plane. The magnitude of x-component and y-component of magnetic NF data \mathbf{H}_x and \mathbf{H}_y are shown in Figs. 6 and 7, respectively. Furthermore, the FF data sampled from 3 m away

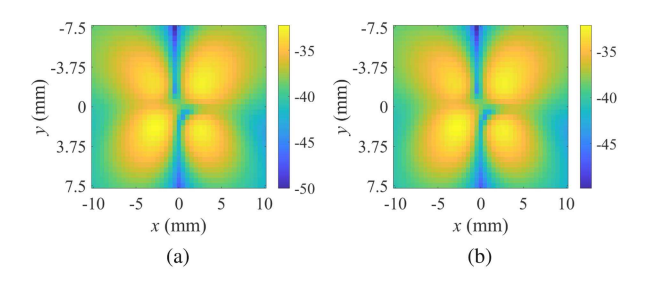


Fig. 6. Magnitude of x-component of the sampled magnetic NF (dB A/m) in the first numerical example at 1.6875 GHz. (a) Magnitude of \mathbf{H}_x calculated by the proposed SRM. (b) Magnitude of \mathbf{H}_x obtained from FEKO simulation.

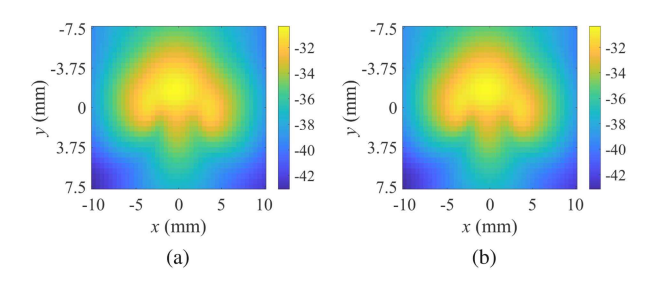


Fig. 7. Magnitude of y-component of sampled magnetic NF (dB A/m) in the first numerical example at 1.6875 GHz. (a) Magnitude of \mathbf{H}_y calculated by the proposed SRM. (b) Magnitude of \mathbf{H}_y obtained from FEKO simulation.

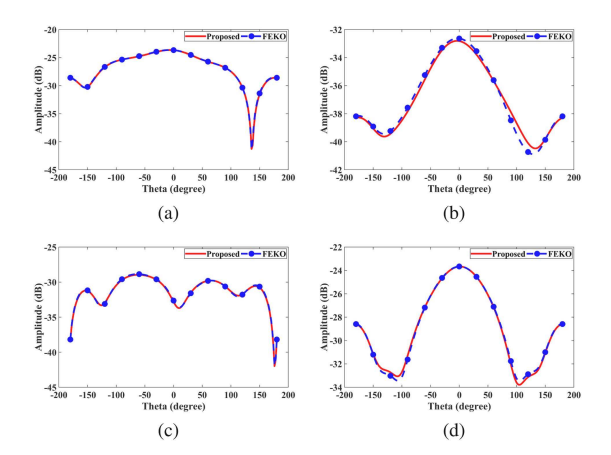


Fig. 8. Magnitude of electric FF (dB V/m) at 3 m away from bottom center of PCB at 1.6875 GHz. (a) and (b) Magnitudes of E_{θ} and E_{ϕ} in the xoz plane, respectively. (c) and (d) Magnitudes of E_{θ} and E_{ϕ} in the yoz plane, respectively.

from the bottom center of the PCB is shown in Fig. 8. In this example, $\sigma_{\rm mse}$ of NF data is -61.20 dB, while $\sigma_{\rm mse}$ of FF at 3 m away is -40.45 dB, respectively. Both the NF and FF calculated by the proposed method agree with FEKO simulation very well.

B. PCB With a Pair of Differential Transmission Lines in a Shielding Enclosure With Multiple Slots

In the second example, a PCB with pair of differential transmission lines placed in a shielding enclosure with multiple slots at top is shown in Fig. 9. Two 1-V voltage sources with 180° difference are terminated at p_1 and p_2 , respectively. Both p_3 and p_4 are loaded with a 50- Ω resistor, which is matched with the source. The thickness of the substrate is 2 mm, and it is made of FR4 material with a relative permittivity of 4.35. It is assumed that the transmission lines on the board have negligible thickness

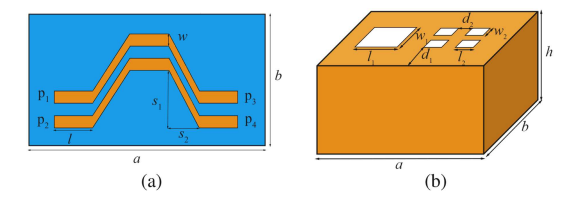


Fig. 9. (a) Geometry of the PCB in the second numerical example (a=10 cm, b=5 cm, l=2 cm, $s_1=2.5$ cm, $s_2=1.75$ cm, and w=3.58 mm). (b) Structure of the shielding enclosure with multiple slots at top (a=15 cm, b=10 cm, h=5 cm, $l_1=6$ cm, $d_1=2$ cm, $w_1=6$ cm, $l_2=1.5$ cm, $d_2=3$ cm, and $w_2=2$ cm).

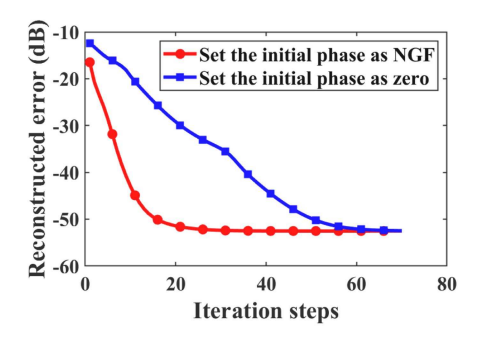


Fig. 10. Reconstructed error (in decibel) of two different phase initialization methods in the second numerical example.

TABLE II
INTERPOLATION ERROR OF THE PROPOSED SRM AT CENTRAL FREQUENCY
POINTS OF EVERY SUBINTERVAL IN THE SECOND NUMERICAL EXAMPLE

f (GHz)	1.125	1.375	1.625	1.8125	1.9375	2.03125
$\sigma(\%)$	3.64	3.37	5.89	1.74	5.25	1.23
f (GHz)	2.09375	2.1875	2.375	2.53125	2.59375	2.65625
$\sigma(\%)$	5.03	0.45	1.98	1.72	5.50	5.10
f (GHz)	2.71875	2.8125	2.9375	3.0625	3.15625	3.21875
$\sigma(\%)$	2.24	4.69	2.08	1.68	0.76	4.91
f (GHz)	3.28125	3.34375	3.4375	3.53125	3.59375	3.6875
$\sigma(\%)$	5.19	4.59	5.14	3.90	4.85	5.33
f (GHz)	3.8125	3.9375				
$\sigma(\%)$	4.68	1.86				

and exhibit ideal conductivity properties. The thickness of the shielding enclosure is set to 2 mm. The PCB board is centrally positioned above the inner bottom of the shielding enclosure. With the resolution of 5 mm, the NF data are obtained from a plane 7 cm above ground plane. The size of the sampled plane is $20 \text{ cm} \times 15 \text{ cm}$.

The comparison of two phase initialization methods in this numerical example is shown in Fig. 10. Our proposed phase initialization method shows a better performance in the convergence of solution of equivalent source. The supporting frequency points in this numerical example f_s are $\{1, 1.25, 1.5, 1.75, 1.875, 2, 2.0625, 2.125, 2.25, 2.5, 2.5625, 2.625, 2.6875, 2.75, 2.875, 3.3125, 3.1875, 3.25, 3.3125, 3.375, 3.5, 3.5625, 3.625, 3.75, 3.875, 4<math>\}$ GHz. The error functions at the midpoints of every subinterval are shown in Table II and the average value of the error function is 3.57%.

To have an intuitive understanding of accuracy of reconstructed equivalent source, the field data calculated by the proposed SRM and FEKO simulation at the frequency 3.9375 GHz are shown in Figs. 11–13. The NF data for validation is sampled

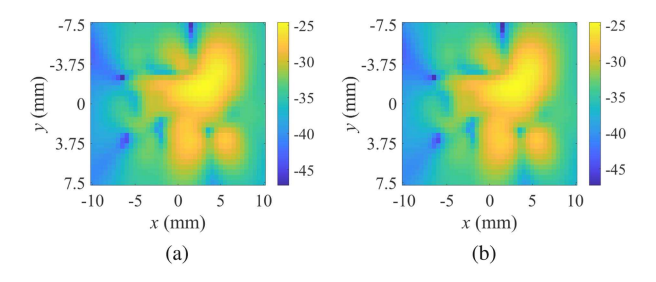


Fig. 11. Magnitude of x-component of sampled magnetic NF (dB A/m) in the second numerical example at 3.9375 GHz. (a) Magnitude of \mathbf{H}_x calculated by the proposed SRM. (b) Magnitude of \mathbf{H}_x obtained from FEKO simulation.

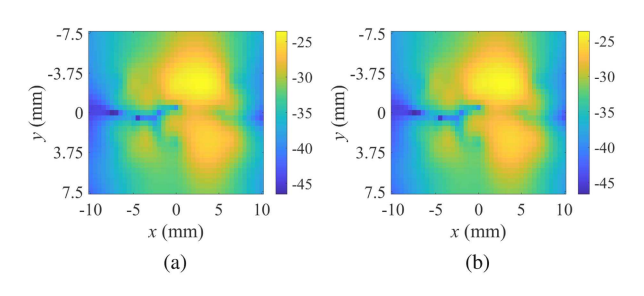


Fig. 12. Magnitude of y-component of sampled magnetic NF (dB A/m) in the second numerical example at 3.9375 GHz. (a) Magnitude of \mathbf{H}_y calculated by the proposed SRM. (b) Magnitude of \mathbf{H}_y obtained from the FEKO simulation.

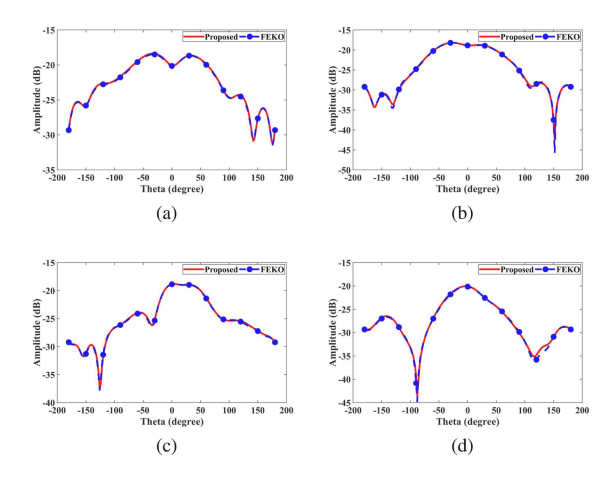


Fig. 13. Magnitude of electric FF (dB V/m) at 3 m away from the bottom center of the PCB at 3.9375 GHz. (a) and (b) Magnitudes of E_{θ} and E_{ϕ} in the xoz plane, respectively. (c) and (d) Magnitudes of E_{θ} and E_{ϕ} in the yoz plane, respectively.

from a plane 6 cm over the ground, while the FF data are sampled from sphere with the radius equal to 3 m. The reconstructed error of NF data in this example is -51.95 dB, while $\sigma_{\rm mse}$ of FF at 3 m away is -41.50 dB. Obviously, the proposed SRM shows great accuracy in both NF and FF reconstruction.

C. PCB With More Complex Structure in a Shielding Enclosure With Multiple Slots and Circular Apertures

In this numerical example, a PCB with more complex circuit structure is shown in Fig. 14(a). The structure of the circuit consists of several straight lines and loops. The ports p_1-p_5 are terminated with a 1-V voltage source, while the ports p_6-p_{10} are

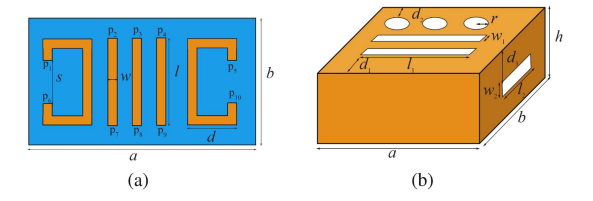


Fig. 14. (a) Geometry of the PCB in the third numerical example ($a=10~{\rm cm}, b=5~{\rm cm}, l=4~{\rm cm}, d=2.5~{\rm cm}, s=2~{\rm cm},$ and $w=3.58~{\rm mm}$). (b) Structure of the shielding enclosure with multiple slots and circular apertures at top and right ($a=15~{\rm cm}, b=10~{\rm cm}, h=5~{\rm cm}, l_1=10~{\rm cm}, d_1=2.32~{\rm cm}, w_1=3.58~{\rm mm}, d_2=2.5~{\rm cm}, r=5~{\rm mm}, l_2=3~{\rm cm}, d_3=1.75~{\rm cm},$ and $w_2=1.5~{\rm cm}$).

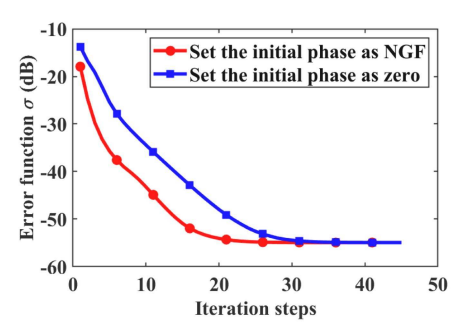


Fig. 15. Reconstructed error (in decibel) of two different phase initialization methods in the third numerical example.

TABLE III
INTERPOLATION ERROR OF THE PROPOSED SRM AT CENTRAL FREQUENCY
POINTS OF EVERY SUBINTERVAL IN THE THIRD NUMERICAL EXAMPLE

f (GHz)	1.125	1.375	1.625	1.875	2.03125	2.09375
$\sigma(\%)$	1.56	4.89	1.85	1.96	5.15	5.41
f (GHz)	2.1875	2.3125	2.40625	2.46875	2.53125	2.59375
$\sigma(\%)$	1.63	0.82	4.59	4.58	5.41	4.53
f (GHz)	2.65625	2.71875	2.8125	2.9375	3.125	3.3125
$\sigma(\%)$	1.56	2.36	2.38	4.22	5.11	5.09
f (GHz)	3.4375	3.53125	3.59375	3.65625	3.71875	3.8125
$\sigma(\%)$	4.77	4.73	4.90	3.44	5.37	5.06
f (GHz)	3.90625	3.96875				
$\sigma(\%)$	4.34	0.28				

loaded with 50- Ω resistors, which are the same as the source resistance. The substrate has a thickness of 2 mm and is composed of FR4 material, which has a ε_r value of 4.35. It is assumed that the transmission lines on the PCB board have infinitesimally thin traces and exhibit perfect conductivity. As shown in Fig. 14(b), the shielding enclosure has multiple slots and circular apertures at the top and right side. A 2-mm thickness is specified for the shielding enclosure. The PCB board is situated at the center, directly above the inner bottom of the shielding enclosure. The NF scanning is implemented on the plane 7 cm over the ground with the resolution of 5 mm.

The comparison of two phase initialization methods in this numerical example is shown in Fig. 15. The set of supporting frequency points f_s are {1, 1.25, 1.5, 1.75, 2, 2.0625, 2.125, 2.25, 2.375, 2.4375, 2.5, 2.5625, 2.625, 2.6875, 2.75, 2.875, 3, 3.25, 3.375, 3.5, 3.5625, 3.625, 3.6875, 3.75, 3.875, 3.9375, 4} GHz. The error function defined in (11) at the midpoints of every subinterval are shown in Table III. The average value of error function is 3.69%.

Compared with the FEKO simulation result, the reconstructed NF data and FF data at the frequency 2.3125 GHz are shown in

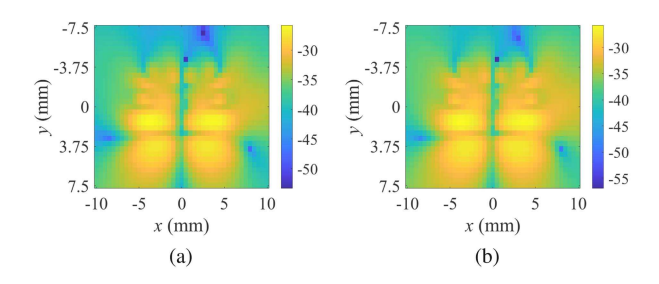


Fig. 16. Magnitude of x-component of sampled magnetic NF (dB A/m) in the third numerical example at 2.3125 GHz. (a) Magnitude of \mathbf{H}_x calculated by the proposed SRM. (b) Magnitude of \mathbf{H}_x obtained from FEKO simulation.

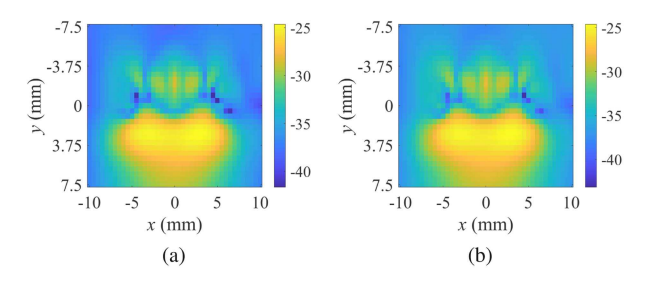


Fig. 17. Magnitude of y-component of the sampled magnetic NF (dB A/m) in the third numerical example at 2.3125 GHz. (a) Magnitude of \mathbf{H}_y calculated by the proposed SRM. (b) Magnitude of \mathbf{H}_y obtained from FEKO simulation.

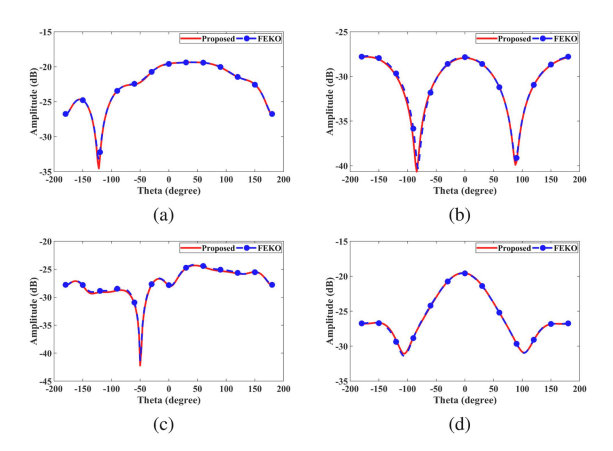


Fig. 18. Magnitude of electric FF (dB V/m) at 3 m away from bottom center of PCB at 2.3125 GHz. (a) and (b) Magnitudes of E_{θ} and E_{ϕ} in the xoz plane, respectively. (c) and (d) Magnitudes of E_{θ} and E_{ϕ} in the yoz plane, respectively.

Figs. 16–18. The NF data for validation are sampled from the plane at the height of 6 cm and the FF data are sampled from sphere with the radius of 3 m. The value of $\sigma_{\rm mse}$ defined in (9) for the NF data are -50.29 dB, and the $\sigma_{\rm mse}$ for the FF at 3 m away is -39.20 dB. Great agreements are achieved for both near- and far-field reconstruction results compared to the FEKO simulation.

D. Study of Influence of Noise

In this section, artificial noise is added to the NF data obtained through FEKO simulations to validate the robustness of the proposed SRM. First, the impact of noise on the proposed SRM at a single frequency is investigated. Taking the example in Section III-A as an illustration, the operating frequency is set as 1.6875 GHz. The input magnetic NF is sampled on a plane

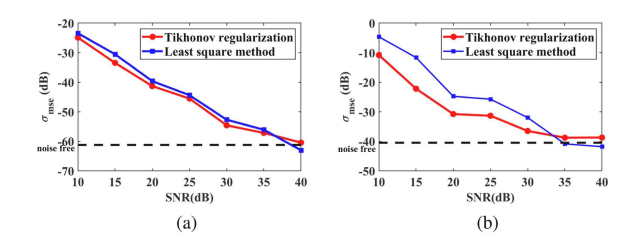


Fig. 19. $\sigma_{\rm mse}$ of near field and far field data in the first numerical example at the frequency of 1.6875 GHz for various SNRs. (a) $\sigma_{\rm mse}$ of NF data. (b) $\sigma_{\rm mse}$ of FF data.

located 6 cm above the ground with the size of 20 cm×15 cm. Gaussian white noise of varying magnitudes is added to the input NF data obtained from FEKO simulations. The signal-to-noise ratio (SNR) range is set from 10 to 40 dB. The NF data for validation are sampled from the plane located 7 cm above the ground, while the FF data for validation are sampled from a sphere 3 m away from the bottom center of the PCB. Then, the $\sigma_{\rm mse}$ of the NF and FF data with the variation of the SNR are shown in Fig. 19. The impact of noise on the accuracy of the reconstructed radiated field increases with the decrease of the SNR. When the SNR drops below 25 dB, the influence of noise becomes significant and cannot be neglected. In addition, the robustness of the Tikhonov regularization method in the proposed SRM is compared with the traditional LSM. It can be observed that the Tikhonov regularization method yields smaller $\sigma_{\rm mse}$ for both NF and FF data compared to the traditional LSM especially for FF data. Similar relationships can be observed for the other numerical examples provided in this article, as well as for different frequency points within the same example.

For the proposed wideband SRM, the introduction of noise at each supporting frequency point can lead to deviations between the reconstructed equivalent source and the theoretical values. As a result, the error of the equivalent source obtained by the interpolation algorithm may be further amplified. To further investigate the impact of noise on the proposed wideband SRM, Gaussian white noise with an SNR of 30 dB is added to the input NF data for each initial sampling frequency point in the numerical example of III-A. Then, the final supporting frequency points f_s obtained by AFS are {1, 1.125, 1.25, 1.375, 1.5, 1.625, 2, 2.25, 2.375, 2.4375, 2.5, 2.5625, 2.625, 2.75, 2.875, 2.9375, 3, 3.125, 3.1875, 3.25, 3.375, 3.4375, 3.5, 3.5625, 3.625, 3.75, 3.875, 4} GHz, which is the same as the ideal case without noise. The average value of interpolation error at the midpoints of the subintervals generated by the aforementioned supported frequency points is 3.98%, which is closed to the value of 3.83% of the case without noise. This indicates that noise has minimal impact on the construction of the interpolation function in the proposed wideband SRM. After adding artificial noise, the $\sigma_{\rm mse}$ of NF and FF data at the frequency of 1.6875 GHz are -54.36and -39.69 dB, respectively. Compared to the FF, the $\sigma_{\rm mse}$ of the NF is more affected by noise, but the accuracy is still within an acceptable range. Therefore, it can be concluded that the proposed wideband SRM exhibits a certain level of robustness.

IV. CONCLUSION

In this article, a wideband SRM based on the magnitude-only NF data is proposed to characterize electromagnetic emission from DUTs placed in shielding enclosure. Only the single-plane NF scanning is needed in the proposed method. Due to the unavailability of the analytical DGF in complex EM environment, the numerical form of the DGF is employed. Tikhonov regularization gathered with GCV is applied to overcome the ill-posed property of the inverse problem. To retrieve phase information from magnitude-only NF data, an iteration method with an assumed initial phase is proposed. Cubic spline interpolation algorithm is used to expand the proposed SRM to a wide working band. In this process, AFS is used to determine supporting frequency points used in interpolation while improving the computational efficiency at the same time. Three numerical examples are shown in this article to validate the effectiveness of proposed method for different structures of circuits and shielding enclosures. The proposed SRM shows a high level of accuracy in both NF and FF reconstruction. The influence of the initial phase of sampled NF data is also investigated, which reveals the effectiveness of the proposed phase initialization method.

REFERENCES

- [1] M. Oswal et al., "Near-field to far-field prediction for high-speed board using an empirical approach," in *Proc. IEEE Electr. Des. Adv. Packag. Syst. Symp.*,, 2010, pp. 1–4.
- [2] C. Gennarelli et al., "Recent advances in near-field to far-field transformation techniques," *Int. J. Antennas Propag.*, vol. 2012, pp. 911–940, Jul. 2012.
- [3] J. L. A. Quijano and G. Vecchi, "Field and source equivalence in source reconstruction on 3 D surfaces," *Progr. Electromagn. Res.*, vol. 103, pp. 67–100, 2010.
- [4] J. Kornprobst, R. A. Mauermayer, O. Neitz, J. Knapp, and T. F. Eibert, "On the solution of inverse equivalent surface-source problems," *Progr. Electromagn. Res.*, vol. 165, pp. 47–65, 2019.
- [5] J. Kornprobst, J. Knapp, R. A. Mauermayer, O. Neitz, A. Paulus, and T. F. Eibert, "Accuracy and conditioning of surface-source based near-field to far-field transformations," *IEEE Trans. Antennas Propag.*, vol. 69, no. 8, pp. 4894–4908, Aug. 2021.
- [6] Y. Alvarez, F. Las-Heras, and M. R. Pino, "On the comparison between the spherical wave expansion and the sources reconstruction method," *IEEE Trans. Antennas Propag.*, vol. 56, no. 10, pp. 3337–3341, Oct. 2008.
- [7] S. Rengarajan and Y. Rahmat-Samii, "The field equivalence principle: Illustration of the establishment of the non-intuitive null fields," *IEEE Antennas Propag. Mag.*, vol. 42, no. 4, pp. 122–128, Aug. 2000.
- [8] J. Li, X.-C. Wei, L. Gao, and Y.-F. Shu, "An effective equivalent radiation source based on near-field scanning for electromagnetic interference estimation," in *Proc. Asia-Pacific Int. Symp. Electromagn. Compat.*, 2017, pp. 315–317.
- [9] X. Tong, D. W. P. Thomas, A. Nothofer, P. Sewell, and C. Christopoulos, "Modeling electromagnetic emissions from printed circuit boards in closed environments using equivalent dipoles," *IEEE Trans. Electromagn. Compat.*, vol. 52, no. 2, pp. 462–470, May 2010.
- [10] P. Li and L. J. Jiang, "Source reconstruction method-based radiated emission characterization for PCBs," *IEEE Trans. Electromagn. Compat.*, vol. 55, no. 5, pp. 933–940, Oct. 2013.
- [11] Z. A. Wang, Z. F. Xiao, J. F. Mao, L. J. Jiang, H. Bagci, and P. Li, "Source reconstruction of electronic circuits in shielding enclosures based on numerical Green's function and application in electromagnetic interference estimation," *IEEE Trans. Microw. Theory Tech.*, vol. 70, no. 8, pp. 3789–3801, Aug. 2022.
- [12] J. Zhang, K. W. Kam, J. Min, V. V. Khilkevich, D. Pommerenke, and J. Fan, "An effective method of probe calibration in phase-resolved near-field scanning for EMI application," *IEEE Trans. Instrum. Meas.*, vol. 62, no. 3, pp. 648–658, Mar. 2013.
- [13] J.-R. Regue, M. Ribo, J.-M. Garrell, and A. Martin, "A genetic algorithm based method for source identification and far-field radiated emissions

- prediction from near-field measurements for PCB characterization," *IEEE Trans. Electromagn. Compat.*, vol. 43, no. 4, pp. 520–530, Nov. 2001.
- [14] B. Wang, E.-X. Liu, W.-J. Zhao, and C. E. Png, "Reconstruction of equivalent emission sources for PCBs from near-field scanning using a differential evolution algorithm," *IEEE Trans. Electromagn. Compat.*, vol. 60, no. 6, pp. 1670–1677, Dec. 2018.
- [15] F.-P. Xiang, E.-P. Li, X.-C. Wei, and J.-M. Jin, "A particle swarm optimization-based approach for predicting maximum radiated emission from PCBs with dominant radiators," *IEEE Trans. Electromagn. Compat.*, vol. 57, no. 5, pp. 1197–1205, Oct. 2015.
- [16] P. Li and L. Jiang, "An iterative source reconstruction method exploiting phaseless electric field data," *Prog. Electromagn. Res.*, vol. 134, no. 1, pp. 419–435, 2013.
- [17] J. Zhang and J. Fan, "Source reconstruction for IC radiated emissions based on magnitude-only near-field scanning," *IEEE Trans. Electromagn. Compat.*, vol. 59, no. 2, pp. 557–566, Apr. 2017.
- [18] J. Wen, L. Ding, Y.-L. Zhang, and X.-C. Wei, "Equivalent electromagnetic hybrid dipole based on cascade-forward neural network to predict nearfield magnitude of complex environmental radiation," *IEEE J. Multiscale Multiphys. Comput. Tech.*, vol. 5, pp. 227–234, Sep. 2020.
- [19] J. Wen, X.-C. Wei, Y.-L. Zhang, and T.-H. Song, "Near-field prediction in complex environment based on phaseless scanned fields and machine learning," *IEEE Trans. Electromagn. Compat.*, vol. 63, no. 2, pp. 571–579, Apr. 2021.
- [20] Y.-F. Shu, X.-C. Wei, R. Yang, and E.-X. Liu, "An iterative approach for EMI source reconstruction based on phaseless and single-plane near-field scanning," *IEEE Trans. Electromagn. Compat.*, vol. 60, no. 4, pp. 937–944, Aug. 2018.
- [21] L. Wang, Y. Zhang, F. Han, J. Zhou, and Q. H. Liu, "A phaseless inverse source method (PISM) based on near-field scanning for radiation diagnosis and prediction of PCBs," *IEEE Trans. Microw. Theory Tech.*, vol. 68, no. 10, pp. 4151–4160, Jul. 2020.
- [22] P. Li, Y. Li, L. J. Jiang, and J. Hu, "A wide-band equivalent source reconstruction method exploiting the Stoer-Bulirsch algorithm with the adaptive frequency sampling," *IEEE Trans. Antennas Propag.*, vol. 61, no. 10, pp. 5338–5343, Oct. 2013.
- [23] T.-H. Song, X.-C. Wei, Z.-Y. Tang, and R. X.-K. Gao, "Broadband radiation source reconstruction based on phaseless magnetic near-field scanning," *IEEE Antennas Wireless Propag. Lett.*, vol. 20, no. 1, pp. 113–117, Jan. 2021.
- [24] Z. A. Wang, L. J. Jiang, J. F. Mao, and P. Li, "Numerical Green's function-based method for modeling radiated emission from PCBs in shielding enclosures," *IEEE Trans. Microw. Theory Tech.*, vol. 69, no. 12, pp. 5250–5258, Dec. 2021.
- [25] J. A. Kong, Electromagnetic Wave Theory. Cambridge, MA, USA: EMW, 2008, pp. 495–498.
- [26] Altair Feko, 2020. [Online]. Available: https://www.altair.com/feko/
- [27] T. Sarkar, D. Weiner, and V. Jain, "Some mathematical considerations in dealing with the inverse problem," *IEEE Trans. Antennas Propag.*, vol. 29, no. 2, pp. 373–379, Mar. 1981.
- [28] J. Colinas, Y. Goussard, and J.-J. Laurin, "Application of the Tikhonov regularization technique to the equivalent magnetic currents near-field technique," *IEEE Trans. Antennas Propag.*, vol. 52, no. 11, pp. 3122–3132, Nov. 2004.
- [29] G. H. Golub and H. G. Wahba, "Generalized cross-validation as a method for choosing a good ridge parameter," *Technometrics*, vol. 21, no. 2, pp. 215–223, 1979.
- [30] G. E. Forsythe, C. B. Moler, and M. A. Malcolm, Computer Methods for Mathematical Computations., Englewood Cliffs, NJ, USA: Prentice-Hall, 1977.
- [31] H. Zhao, Y. Zhang, J. Hu, and Z. Chen, "Estimation of initial guess of steepest descent method for near field phase retrieval," in *Proc. Asia-Pac. Int. Symp. Electromagn. Compat.*, 2017, pp. 306–308.



Zhifei Xiao received the B.S. degree in information engineering, in 2021, from Shanghai Jiao Tong University, Shanghai, China, where she is currently working toward the master's degree in electronics and communication engineering.

Her research interests include electromagnetic compatibility modeling and source reconstruction method.



Zi An Wang (Graduate Student Member, IEEE) was born in Xuzhou, Jiangsu, China, in 1999. He received the B.S. degree in electronic information science and technology from the University of Electronic Science and Technology of China (UESTC), Chengdu, China, in 2020. He is currently working toward the Ph.D. degree in electronic science and technology with Shanghai Jiao Tong University, Shanghai, China.

His research interests include electromagnetic compatibility/electromagnetic interference modeling, inverse source reconstruction method, and its

application in characterization and design.



Li Jun Jiang (Fellow, IEEE) received the B.S. degree in electrical engineering from the Beijing University of Aeronautics and Astronautics, Beijing, China, in 1993, the M.S. degree in electrical engineering from Tsinghua University, Beijing, China, in 1996, and the Ph.D. degree in electrical engineering from the University of Illinois at Urbana—Champaign, Champaign, IL, USA, in 2004.

He has plenty of experience in both academia and industry. His multidisciplinary research activities have resulted in leading research outputs around 170

peer-reviewed journal publications, many international and regional awards, multiple patents, and book/book chapters. His ultimate research objective is to explore first principle-based methodologies for complex multidisciplinary scientific and engineering challenges. From 1996 to 1999, he was an Application Engineer with the Hewlett-Packard Company (HP). From 2004 to 2009, he has been the Postdoctoral Researcher, Research Staff Member, and Senior Engineer with IBM T.J. Watson Research Center, New York, NY, USA. He was an Associate Professor from December 2009, and then, the Honorable Associate Professor with the Department of Electrical and Electronic Engineering, University of Hong Kong (HKU), Hong Kong, where he received tenure in July 2014. From June 2013 to June 2014, he was the Senior Visiting Professor with Tsinghua University, Beijing, China. From 2014 to 2018, he was an occasional Visiting Scholar to Prof. T. Itoh's group with the University of California, Los Angeles, Los Angeles, CA, USA, where he spent his sabbatical from 2014 to 2015. In 2022, he joined the Department of Electronic Engineering, Chinese University of Hong Kong, Hong Kong, as a Professor. His research interests include electromagnetics, heterogeneous electromagnetic modeling methodologies, electronic physical design EDA solutions including signal integrity/power integrity and electromagnetic compatibility/electromagnetic interference, antenna and microwave technologies, electromagnetic engineering for linear and nonlinear artificial materials, nanostructures, Terahertz, optics, etc.

Dr. Jiang was the recipient of the IEEE MTT Graduate Fellowship Award in 2003 and the Y. T. Lo Outstanding Research Award in 2004. He is a Member of the IEEE Antennas and Propagation Society, the IEEE Microwave Theory and Technology Society, the IEEE Electromagnetic Compatibility Society, the Applied Computational Electromagnetics Society (ACES), and the Chinese Computational Electromagnetics Society. He has been an elected technical program committee (TPC) Member of the IEEE Electrical Design of Advanced Packaging and Systems Symposium (EDAPS) since 2010, and the IEEE Electrical Performance of Electronic Packaging since 2014. He was a TPC Member of the 2013 IEEE International Conference on Microwave Technology and Computational Electromagnetics. He has been a TC-9 Member and a TC-10 Member of the IEEE Electromagnetic Compatibility Society since 2011. He was a Scientific Committee Member of the 2010 IEEE Simulation and Modeling of Emerging Electronics, the Special Session Organizer of the IEEE EDAPS, the IEEE Electromagnetic Compatibility, ACES, Asia-Pacific Radio Science Conference, Progress in Electromagnetics Research Symposium, and a Co-Organizer of the HKU Computational Science and Engineering Workshops from 2010 to 2012. He was a Session Chair of many international conferences. He was the TPC Chair of the 7th International Conference on Nanophotonics/the 3rd Conference on Advances in Optoelectronics and Micro/Nano Optics, the TPC Co-Chair of the 12th International Workshop on Finite Elements for Microwave Engineering and the 2013 International Workshop on Pulsed Electromagnetic Field at Delft, The Netherlands, and the General Chair of the 2014 IEEE 14th HK AP/MTT Postgraduate Conference.



Ping Li (Senior Member, IEEE) received the B.S. degree in physical electronics engineering and the master's degree in microwave engineering from the University of Electronic Science and Technology of China (UESTC), Chengdu, China, in 2008 and 2010, respectively, and the Ph.D. degree in electrical and electronic engineering from the University of Hong Kong (HKU), Hong Kong, in 2014.

From 2014 to 2015, he was a Postdoctoral Fellow with the Computational Electromagnetics Lab, King Abdullah University of Science and Technology

(KAUST), Thuwal, Saudi Arabia. From 2015 to 2016, he was a Postdoctoral Fellow with the On-Chip Electromagnetics Lab, Purdue University, West Lafayette, IN, USA. From 2017 to 2018, he was with the Department of Electrical and Electronic Engineering, HKU, as a Research Assistant Professor. From September 2018 to August 2019, he was a Research Scientist with KAUST, as well as a Honorary Assistant Professor with HKU. Since 2019, he has been with Shanghai Jiao Tong University as an Associate Professor.

Dr. Li was the recipient of the 2018 Joint IEEE EMC and APEMC Outstanding Young Scientist Award, 2018 ACES-China Young Scientist Award, and 40th PIERS Young Scientist Award in Japan. He was the recipient of the Okawa Research Foundation Grant of Japan. Besides, he was the recipient of 2018 Best Annual Paper Prize on *Chinese Journal of Radio Science*, and the recipient of Second Prize Award for the Natural Sciences of Chinese Institute of Electronics, 2019. Besides, his paper was selected as the Finalist paper in 29th International Review of Progress in Applied Computational Electromagnetics and 2014 International Symposium on Electromagnetic Compatibility, and he was the recipient of the Best Student Paper Award in 12th International Workshop on Finite Elements for Microwave Engineering.